Adaptive identification of lowpass filter cutoff frequency for online vessel model tuning

Xu Han [*], Zhengru Ren, Bernt Johan Leira, Svein Sævik

Department of Marine Technology, Norwegian University of Science and Technology (NTNU), 7491 Trondheim, Norway
Centre for Research-based Innovation on Marine Operations (SFI MOVE), Norway

A R T I C L E   I N F O

A B S T R A C T

Tuning of vessel models in real-time based on vessel measurements and weather information is of great interest in order to increase the safety and efficiency of marine operations. Vessel motion signals usually contain high-frequency noise. For an unbiased model tuning algorithm, it is essential to filter the noisy signals in order to identify the power of the wave-induced first-order vessel response. Lowpass filters with high accuracy should therefore be applied. However, it is a challenge to design such a filter since the optimal cutoff frequency can vary with sea states, vessel dimensions, vessel conditions, etc. This paper proposes a novel algorithm to adaptively search for the optimal cutoff frequency for a lowpass filter with high accuracy. The algorithm is fundamentally based on the facts that the vessel naturally acts as a lowpass filter and the energy from the high-frequency components, e.g., signal noise, is significantly smaller than that from the wave-induced vessel response. The algorithm is validated by 500 numerically simulated vessel motion signals with quite high noise levels and also by analysis of several on-site full-scale vessel motion signals. The improvements to the tuning results for the vessel parameters are demonstrated.

1. Introduction

Marine operations are usually designed onshore before they are executed. Operational limits are determined based on presumed operational scenarios, loading conditions, etc. Practically, it is common to calculate the wave-induced loads and motions based on linear transfer functions, named response amplitude operators (RAOs) (DNVGL-ST-N001, 2016). However, the applied RAOs at the design stage may not represent the true vessel conditions during operation in an adequate manner, because (1) conservative engineering assumptions are usually made to cover the variation of vessel loading conditions during marine operations, e.g., pipe laying; and (2) the onboard vessel loading condition (inertia distribution) may deviate from the presumed one.

These limitations could lead to over-conservative and inefficient marine operations, or even risky operations with increased possibility of accidents. Therefore, a dynamically adaptive tuning of vessel numerical models could continuously help to improve the knowledge on the real-time vessel condition, and hence increase the efficiency and safety of the marine operations. Han et al. (2021a) proposed an algorithm based on Bayesian inference to improve the knowledge about these real-time vessel conditions and to reduce the model uncertainty quantitatively by using (1) onboard data from sensor systems, e.g., motion reference unit (MRU) and global navigation satellite system (GNSS); (2) wave

information such as H_s (significant wave height), T_p (spectral peak period), β_W (wave direction), directional spreading, and spectral shape. As explained in Han et al. (2021a), tuning of a vessel hydrodynamic model is a multi-modal, multi-dimensional, and nonlinear problem.

The vessel motion measurements are extremely important for many onboard systems, e.g., dynamic positioning (DP) systems and active heave compensators (AHCs). A typical MRU system uses measurements from an inertial measurement unit (IMU) which consists of accelerometers measuring translational accelerations and gyroscopes measuring rotational velocities. It is well recognized that all measurements are inexact but usually they can statistically represent the true value (Hubbard, 2014). The accuracy and precision of the measurements depend on the involved methods, processes, and instruments. IMU measurements may contain errors due to misalignment, mis-scaling, constant and slow-varying biases, gravity-related terms, and nonlinearities from the gyro torque and accelerometers (Grewal et al., 1991). Sensor fusion and signal filtering techniques should therefore be applied to achieve high-fidelity motion monitoring, reduce sensor noise, and avoid measurement drift (Fossen, 2011).

Filters can be categorized into model-free and model-based approaches, depending on whether a representative model is applied. Kalman filters and the associated extended methods have been the most

Nomenclature

α_j	Sensor screening ratio (SSR) for sensor j
$\bar{x}_j$	The mean of the measured filtered time series for sensor j
β_{44}	Ratio between the additional roll damping and the critical roll damping
β_W	Wave direction w.r.t. vessel coordinate system
$\eta_{33}, \dot{\eta}_{33}, \ddot{\eta}_{33}$	Heave displacement, velocity, acceleration
γ_p	Peak enhancement factor
$\hat{\sigma}_j\left(f_{lp}\right)$	The standard deviation of signal from sensor j after filtered at cutoff frequency f_{lp}
$\hat{\sigma}_X$	The filtered vessel motion signal STD
$\hat{T}_z$	The zero-upcrossing period of the filtered vessel motion signal
$\hat{x}_j(t)$	The filtered time series for sensor j at time step t
ω	Wave frequency
ω_p	Wave spectral peak frequency
$\overline{\overline{W}}_j$	The weight matrix (likelihood function) based on the received measurements from sensor j
Φ_m	The uncertain vessel parameter to be tuned, $m \in \{1, 2, ..., M\}$
σ_X^*	The true vessel motion signal STD
σ_N^2	Variance of noise
σ_X^2	Variance of response
$\sigma_{\sigma_{r,j}}$	The STD of $\sigma_{r,j}$ over $r \in \{1, 2, ..., N_{RAO}\}$
$\sigma_{r,j}$	The predicted STD by using $RAO_{r,j}$
f_{lp}^*	The optimal cutoff frequency [Hz] for a lowpass filter
f_{lp}	Lowpass filter cutoff frequency [Hz]
$H\left(\omega, \beta_W\right)$	Linear transfer function between wave and vessel (heave) response, i.e. RAO
H_s	Significant wave height
Im	The number of the discrete values used for RAO database for the vessel parameter Φ_m
im	The imth value of the variable Φ_m in the RAO database
j	Sensor ID, the jth sensor, representing different quantities (displacement, velocity, acceleration) and locations
Km	The number of the discrete values use for the probability distribution model for the vessel parameter Φ_m
km	The kmth value of the discretized variable Φ_m in the probability distribution model
M	The number of considered variables for tuning
N_ω	The number of discretized frequencies
N_t	The number of discretized time steps
N_{Prob}	The total number of the discrete points for the joint probability distribution model, $N_{Prob} = \prod_{m=1}^{M}(Km)$
N_{RAO}	The total number of possible vessel parameter combinations to build the RAO database, $N_{RAO} = \prod_{m=1}^{M}(Im)$
p	Power parameter
$P^{(n)}\left(\Phi_1, ..., \Phi_M\right)$	The updated discrete joint probability distribution after the nth updating step
r_{55}	Pitch radius of gyration
$RAO_{r,j}$	The RAO based on the variable combination r, for the sensor j (location and quantity)
$S_{\zeta\zeta}^+\left(\omega, \beta_W\right)$	Single-sided power spectral density of long-crested waves
$S_{XX}^+(\omega)$	Single-sided power spectral density of vessel response X
T_p	Spectral peak period
T_z	Zero-upcrossing period
$w_{r,j}$	Weight factor for the rth variable combination based on measurement from sensor j
$x_j(t)$	The original signal for sensor j at time step t
FFT	Fast Fourier transform
GMT	Correction to the transverse metacentric height due to free surface effects
IMU	Inertial measurement unit
MRU	Motion reference unit
OSV	Offshore supply vessel
PDF	Probability density function
PM	Pierson–Moskowitz spectrum
RAO	Response amplitude operator
SNR	Signal-to-noise ratio
STD	Standard deviation
WN	White noise
XCG	Longitudinal coordinate of vessel center of gravity

popular model-based approaches, due to their convenient formulation

for state estimation and feasibility in relation to time-varying systems

in the time domain (Simon, 2006). Most MRU applications use model-based advanced Kalman filters for the convenient applications of sensor fusion. Ren et al. (2019) proposed motion estimation algorithms by fusing the IMU and GNSS measurements. Grewal et al. (1991) introduced a dual extended Kalman filter for estimating the measurement errors from gyroscopes and accelerometers separately. The separated filtering of gyro and accelerometer measurements reduces the number of coefficients to be tuned. Besides, significant amounts of motion estimation algorithms have been developed based on various Kalman filters, such as unscented Kalman filter (Zhang et al., 2005), adaptive Kalman filter (Li and Wang, 2013), and exogenous Kalman filter (Stovner et al., 2018). An alternative type of model-based filtering technique is based on the Lyapunov stability concept (Fossen and Strand, 1999; Grip et al., 2015). The residual error converges to zero or a bounded region according to online approximation and adaptive updating.

Taking advantage of their simple form, model-free filter techniques are easier to apply. Usually, one is interested to extract the signals within a certain frequency range by applying a bandpass, notch, low-pass, or highpass filter. Many different signal filters have been developed and applied in different fields, e.g., Butterworth filters (Butterworth, 1930) and Kolmogorov filters (Challa and Bar-Shalom, 2000). However, the cutoff frequency should be designed and tuned, either explicitly or implicitly in the filter models. As the first statistically designed filter, the Wiener filter (Wiener, 1964) can optimally extract the true signal from noise within the frequency domain by designing the
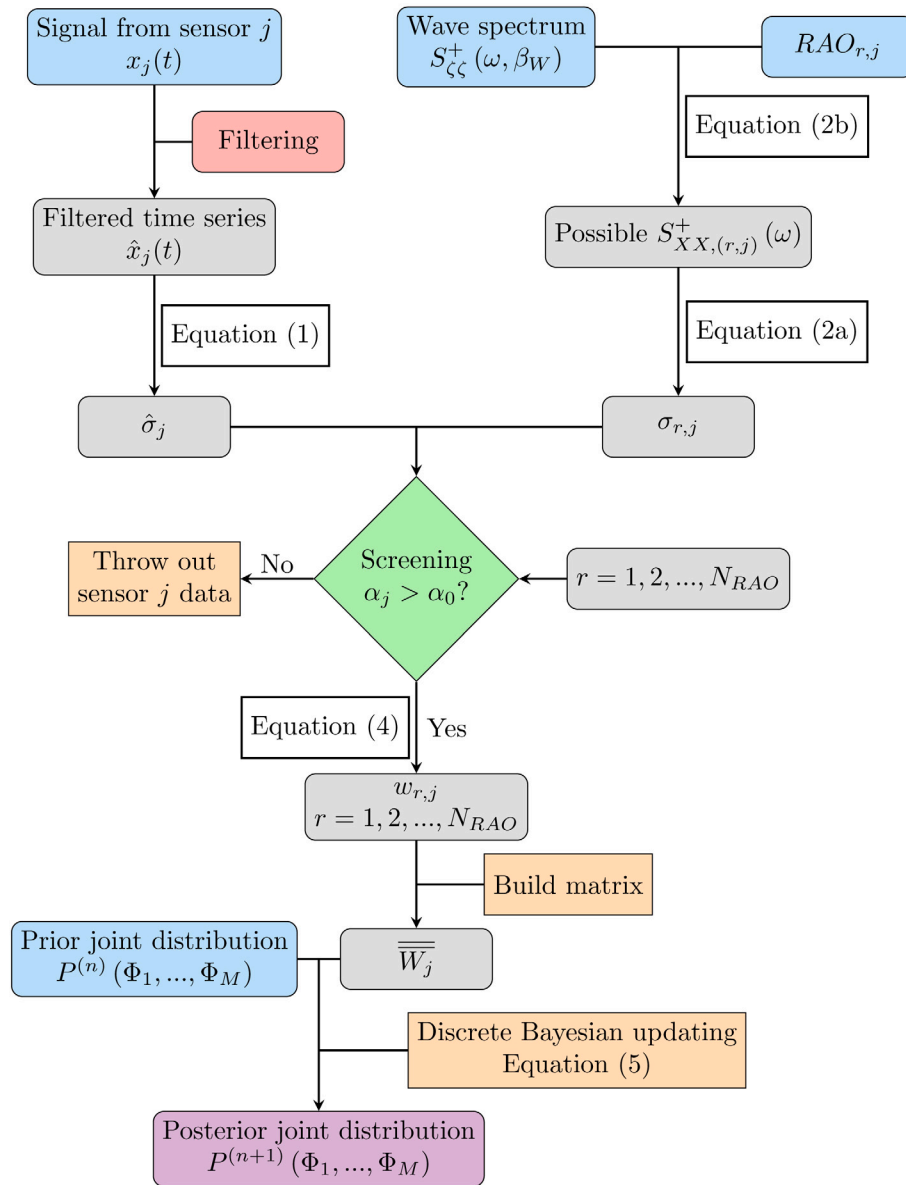
Fig. 1. Process of tuning vessel hydrodynamic model parameters, based on the vessel motion measurements and wave spectrum. Precise knowledge about wave spectrum is assumed.

filter as a linear time-invariant system, requiring knowledge about the noise-free signal spectrum and the noise spectrum. For processing with heave motion measurements, Godhaven (1998) proposed an adaptive highpass filter where the optimal cutoff frequency was obtained by minimizing the measurement errors, which depends on the measured wave condition, the selected filter model and filter order, the considered error sources, etc.

Parametric sensitivity studies of the vessel model tuning algorithm proposed by Han et al. (2021a) showed that the quality of the tuned results highly relies on a reliable filtering of signal noise to identify the vessel motion energy in the wave frequency region. Assuming that the noise energy is mainly within the high-frequency region, a lowpass filter should therefore be applied to remove the high-frequency components (e.g., noises) from the vessel motion signals. Its optimal cutoff frequency depends on many parameters such as sea state, vessel advancing speed, vessel heading, etc. This paper focuses on developing an adaptive algorithm to find the optimal cutoff frequency for the lowpass filter.

The paper is organized as follows. Section 2 briefly describes the procedures of the proposed model tuning algorithm. Section 3 describes the basic inputs of the performed analyses and the scope of work to find an algorithm or a function which could calculate the optimal cutoff frequency. Being the core of this paper, Section 4 aims to identify the important parameters correlated to the optimal cutoff frequency and explore the properties associated with the signals and the cutoff frequencies. Consequently, a novel algorithm is then proposed in Section 4, which can adaptively tune the optimal cutoff frequencies. Then the proposed algorithm is verified by means of 500 randomly generated time series in addition to several on-site vessel motion measurements, described in Section 5. The influence of the proposed adaptive lowpass filter on the vessel model tuning results is then evaluated. Conclusions and future work are presented in Section 6.

2. Basic vessel model tuning procedure

The considered vessel seakeeping model tuning procedure proposed by Han et al. (2021a) is briefly repeated in this section and illustrated in Fig. 1. The joint probability distribution of the uncertain vessel parameters ($\Phi_1, \ldots, \Phi_m, \ldots, \Phi_M, m \in \{1, 2, \ldots, M\}$), after tuning

n times based on the proposed tuning procedure can be expressed as $P^{(n)}\left(\Phi_1, \Phi_2, \ldots, \Phi_M\right)$. The update is based on the provided wave information, vessel motion measurements (e.g., at a sensor numbered as j), and a prepared RAO database which covers all the considered sensors and the whole uncertainty ranges of the considered vessel parameters:

1. Filter the vessel motion measurements from sensor j, $x_j(t)$. In reality, the raw motion signal includes noise in the high-frequency range, a low-frequency signal bias, and environment-induced low-frequency motions. It is important to filter out such disturbances and to identify the first-order wave-induced motions.

2. Calculate the standard deviation (STD) of the filtered signal, $\hat{\sigma}_j$, by

$$\hat{\sigma}_j = \sqrt{\frac{\sum_{t=1}^{N_t}\left(\hat{x}_j(t) - \bar{x}_j\right)^2}{N_t - 1}} \tag{1a}$$

$$\bar{x}_j = \frac{\sum_{t=1}^{N_t} \hat{x}_j(t)}{N_t} \tag{1b}$$

where $\hat{x}_j(t)$ means the estimated time series of the filtered signal for sensor j at the time step t, N_t is the total number of discrete time steps of the signal, and $\bar{x}_j$ is the mean value of the filtered signal.

3. Calculate the standard deviations of the possible vessel response $\sigma_{r,j}$, based on the corresponding wave spectrum and the candidate RAO from the RAO database

$$\sigma_{r,j} = \sqrt{\sum_{n=1}^{N_\omega} S_{XX,(r,j)}^+(\omega_n) \cdot \Delta\omega} \tag{2a}$$

$$S_{XX,(r,j)}^+(\omega) = \left|H_{r,j}(\omega, \beta_W)\right|^2 \cdot S_{\zeta\zeta}^+(\omega, \beta_W) \tag{2b}$$

where N_ω is the total number of discretized frequencies for the response spectrum, $S_{XX,(r,j)}^+(\omega)$ is the spectrum for response X, $S_{\zeta\zeta}^+(\omega, \beta_W)$ is the long-crested wave spectrum without considering directional spreading. S^+ means single-sided power spectrum, $H_{r,j}(\omega, \beta_W)$ represents the RAO candidate calculated based on vessel parameter combination r for sensor j. Each possible combination of the considered vessel parameters, i.e., $\left(\Phi_{i1}, \Phi_{i2}, \ldots, \Phi_{iM}\right)$, is subscripted with number $r \in \{1, 2, \ldots, N_{RAO}\}$, where $N_{RAO} = \prod_{m=1}^{M} Im$ is the total number of vessel parameter combinations and Im is the number of the discretized values of the considered uncertain vessel parameter Φ_m. The possible response STD with the rth combination of parameters for the sensor j is denoted by $\sigma_{r,j}$.

4. Screen out insensitive sensor measurements with respect to the considered vessel model parameters for the current sea state. A new parameter α_j, named sensor screening ratio (SSR), is introduced

$$\alpha_j = \frac{\sigma_{\sigma_{r,j}}}{\hat{\sigma}_j} \tag{3a}$$

$$\sigma_{\sigma_{r,j}} = \sqrt{\frac{\sum_{r=1}^{N_{RAO}}\left(\sigma_{r,j} - \bar{\sigma}_{R,j}\right)^2}{N_{RAO} - 1}} \tag{3b}$$

$$\bar{\sigma}_{R,j} = \frac{\sum_{r=1}^{N_{RAO}} \sigma_{r,j}}{N_{RAO}} \tag{3c}$$

where $\sigma_{\sigma_{r,j}}$ is the STD of $\sigma_{r,j}$ for $r \in \{1, 2, \ldots, N_{RAO}\}$. The previous study used a screening criterion of $\alpha_0 = 0.05$. For a certain sensor j, if $\alpha_j < 0.05$, then the sensor j will be excluded when updating the parameters. SSR basically represents how important the considered vessel parameters are under the current sea state at sensor j.

5. Calculate the weight factor for each $\sigma_{r,j}$ by

$$w_{r,j} = \frac{1}{\left|\sigma_{r,j} - \hat{\sigma}_j\right|^p} \tag{4}$$

where $p \in \mathbb{R}^+$ is called the power parameter. The choice of p value depends on the number of dimensions (M) for the model tuning, the sensitivity and uncertainty range of the considered vessel parameters, and the engineering judgment.

6. Establish the weight matrix $\overline{\overline{W_j}}$, i.e., the likelihood function, for all possible combinations of vessel parameters in the RAO database. The weight matrix has the size of $I1 \times I2 \times \cdots \times IM$.

7. Linearly interpolate the weight matrix $\overline{\overline{W_j}}$ from the size of $I1 \times I2 \times \cdots \times IM$ (variable resolution in the RAO database) to the size of $K1 \times K2 \times \cdots \times KM$ (variable resolution in the discrete joint probability distribution model).

8. Update the joint probability distribution $P^{(n+1)}\left(\Phi_1, \Phi_2, \ldots, \Phi_M\right)$ by multiplying the prior discrete joint probability density with the weight matrix $\overline{\overline{W_j}}$ element-wise

$$PDF^{(n+1)}\left(\Phi_1, \ldots, \Phi_M\right) = \mathcal{NO}\left(PDF^{(n)}\left(\Phi_1, \ldots, \Phi_M\right) \odot \overline{\overline{W_j}}\right) \tag{5}$$

where PDF means the probability density function, $\odot$ operator means the element-wise multiplication of two matrices, i.e., a Hadamard product (Scheick, 1997). $\mathcal{NO}(\cdot)$ is a normalization operator, so that the sum of the probabilities in the joint probability distribution remains 1.0 after every tuning.

The main idea is to transfer the objective of recursively calculating direction-dependent vessel motion RAOs based on vessel motion measurements and wave information to the statistical inference on the vessel model parameters which are direction-independent. The benefits are (1) the tuned results also indicate the confidence; (2) the tuned results can be used to predict the future vessel responses for different sea states and wave directions.

3. Problem statement

Early case studies (Han et al., 2021a) indicated the key role of signal filtering for unbiased vessel model tuning results. Both over-filtering and under-filtering of signal noise could lead to biased tuning results. The high-frequency components of the motion signal which are mainly due to the signal noise and the local vibrations can be removed by a lowpass filter. For the lowpass filter, it is essential to find the optimal cutoff frequency which depends on the sea state, vessel dimension, and vessel condition. However, the wave spectrum can be represented in terms of a number of parameters, such as H_s, T_p, β_W, wave spreading and spectral shape which in reality may not be accurately described by any of the well-known wave spectral types, e.g., Pierson–Moskowitz (PM), JONSWAP, and Thorsethaugen. Therefore, it is difficult to find a general function relating the optimal cutoff frequency to the sea state, vessel dimensions, and vessel condition. In addition, due to the random nature of signal noises, mathematically accurate expression for the function of the optimal cutoff frequency f_{lp}^* becomes a challenge.

This paper focuses on finding the optimal lowpass filter cutoff frequency (f_{lp}^*) in order to estimate the energy of the true wave-induced first-order vessel motion as accurately as possible. The signals are assumed to have no low-frequency components, and therefore only a lowpass filter was required for the signal. With the ambition of finding relations between sea states and f_{lp}^*, the analysis scope described in Section 3.2 is performed. All the analyses were based on one selected vessel with several sensor systems as described in Section 3.1.
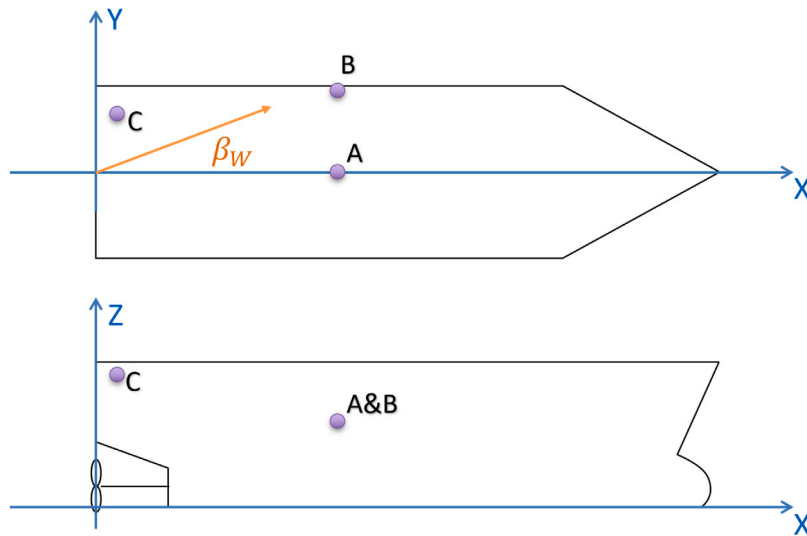
Fig. 2. Illustration of vessel coordinate system and locations of considered measurement points.

Table 1
Vessel information, base case.

Parameters	Description	Value	Unit
L_{PP}	Length between perpendiculars	~120	m
B	Breadth	~27	m
D (Ballast)	Draft	~5.1	m

Table 2
Range of vessel model parameters in RAO database.

Parameters	Variation range	Number of values
Mass	[−6%, +6%]	7
XCG	[−4 m, +4 m]	5
r_{55}	[−9%, +9%]	7
GMT[a]	[0, 1 m]	6
β_{44}	[2%, 14%]	7

[a]Here "GMT" represents the free surface correction to the transverse metacentric height. $GMT = 0.5$ m here means that the transverse metacentric height is corrected with −0.5 m due to free surface effects. It is not the value of the transverse metacentric height.

Table 3
Description of sensor measurements.

Sensor ID	Location	Coordinate (x,y,z) [m]	Signal/measurements
Disp_A	A	(60.0, 0.0, 10.0)	$\eta_{33}(t)$ at location A
Disp_B	B	(60.0, 13.0, 10.0)	$\eta_{33}(t)$ at location B
Disp_C	C	(0.0, 10.0, 14.0)	$\eta_{33}(t)$ at location C
Vel_A	A	(60.0, 0.0, 10.0)	$\dot{\eta}_{33}(t)$ at location A
Vel_B	B	(60.0, 13.0, 10.0)	$\dot{\eta}_{33}(t)$ at location B
Vel_C	C	(0.0, 10.0, 14.0)	$\dot{\eta}_{33}(t)$ at location C
Acc_A	A	(60.0, 0.0, 10.0)	$\ddot{\eta}_{33}(t)$ at location A
Acc_B	B	(60.0, 13.0, 10.0)	$\ddot{\eta}_{33}(t)$ at location B
Acc_C	C	(0.0, 10.0, 14.0)	$\ddot{\eta}_{33}(t)$ at location C

$\eta_{33}(t)$: time series of heave displacement;
$\dot{\eta}_{33}(t)$: time series of heave velocity;
$\ddot{\eta}_{33}(t)$: time series of heave acceleration.

3.1. Vessel model

The numerical studies are based on an offshore supply vessel (OSV) close to its ballast condition (Han et al., 2021a). The primary vessel dimensions are summarized in Table 1. The vessel reference coordinate system moves steadily at the vessel forward speed, as illustrated in Fig. 2. The positive X-axis along the longitudinal symmetric axis points from the stern to the bow ($X = 0$ aft), the Z-axis is pointing vertically upwards from the keel ($Z = 0$), and the Y-axis is normal to the X–Z plane where $Y = 0$ is at the vessel longitudinal symmetry plane. The wave direction β_W follows the same coordinate system, i.e. waves at 180° heading propagate along the negative X-axis.

The RAO database was established (1) to generate signals for different locations and responses of the vessel; and (2) to evaluate the effects of the adaptive lowpass filter on the model tuning performance. Based on the early sensitivity studies of the hydrodynamic model parameters in relation to the vessel motions of interest (Han et al., 2020), variation of five vessel parameters was considered for the RAO database. The considered uncertainty ranges are summarized in Table 2. The discrete values for each parameter are evenly distributed within its uncertainty range. Seakeeping analyses were performed by Wasim (DNV, 2018) (from the DNV Sesam family), applying the Rankine panel method (Kring, 1994). Running analyses through all wave periods in the time domain, the outputs can then be transferred to the frequency domain in order to build the RAOs. A RAO database was then established by considering all possible combinations of the discrete values for the five vessel parameters. Heave responses are often of interest for marine operations (e.g., heavy lift). Therefore, heave RAOs (i.e. displacement, velocity and acceleration) at three different locations (see Fig. 2) were included in the RAO database, for each combination of vessel parameters. As described in Table 3, 9 different measured quantities (sensors) associated with heave response were considered in the model tuning simulations. Only zero advancing speed

was considered for simplicity in order to avoid dealing with the 3-to-1 mapping problem between the absolute wave frequency and encounter frequency for following waves (Lewandowski, 2004). In total, 13 Wave headings between 0° and 180° with a 15° interval were considered in the RAO database for the 9 sensor measurements.

3.2. Finding the optimal cutoff frequency

It is assumed that the high-frequency signal errors can be represented by white noise

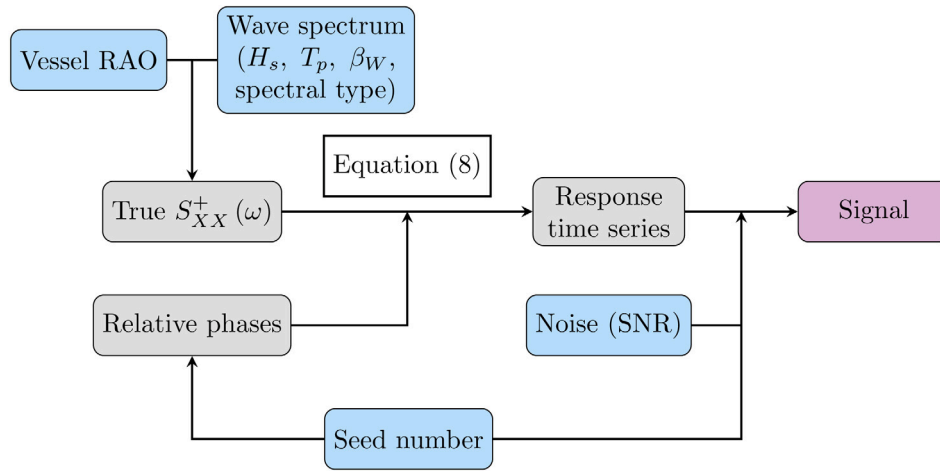$$WN \sim \mathcal{N}\left(0, \sigma_N^2\right) \tag{6}$$

Fig. 3. Flow chart for the purpose of simulating noisy vessel response measurements.. (For interpretation of the references to colour in this figure legend, the reader is referred to the web version of this article.)

where the variance of the noise σ_N^2 is determined by the signal-to-noise ratio (SNR)

$$SNR = \frac{\sigma_X^2}{\sigma_N^2} \tag{7}$$

where σ_X^2 is the variance of the true signal.

The response signal can be simulated according to the process in Fig. 3. Blocks in blue are the required inputs which together can uniquely determine the output signal. The seed number was used to generate both the relative phase φ_n for each frequency component ω_n and the noise for each time step. A massive amount of vessel heave motion signals were generated by varying all the input parameters in Fig. 3, in order to investigate the relations between inputs and f_{lp}^*.

The considered variation of inputs are summarized in Table 4. Each simulation lasts for 1 h. The time series were generated based on the corresponding response spectrum by application of the following relationships:

$$x(t) = \sum_{n=1}^{N_\omega} C_n(\omega_n) \cos(\omega_n t + \varphi_n) \tag{8a}$$

$$C_n(\omega_n) = \sqrt{2S_{XX}^+(\omega_n) \cdot \Delta\omega} \tag{8b}$$

$$S_{XX}^+(\omega) = |H_X(\omega, \beta_W)|^2 \cdot S_{\zeta\zeta}^+(\omega, \beta_W) \tag{8c}$$

where $\varphi_n \in [0, 2\pi]$ is a random phase angle which is continuous and uniformly distributed, $\Delta\omega$ is the width of the radial frequency interval of ω_n, and N_ω is the total number of the discrete frequencies for the response spectrum. $S_{XX}^+(\omega_n)$ is the single-sided response spectrum for the response X, calculated by Eq. (8c). $|H_X(\omega, \beta_W)|$ is the RAO of the response X for a specific vessel condition. The vessel condition in the present paper is defined by the 5 vessel parameters in Table 2. One vessel condition was randomly selected among the RAO database for the studies of finding the optimal cutoff frequency. $S_{\zeta\zeta}^+(\omega, \beta_W)$ is the wave spectrum. The influence of wave spectral type on the optimal cutoff frequency was studied where three wave spectral types (DNVGL-RP-C205, 2017) were considered, i.e., PM, JONSWAP, and Torsethaugen.

The PM wave spectrum $S_{PM}(\omega)$, originally proposed for fully-developed sea, can be calculated based on H_s and T_p:

$$S_{PM}(\omega) = \frac{5}{16} H_s^2 \omega_p^4 \omega^{-5} \exp(-\frac{5}{4}(\frac{\omega}{\omega_p})^{-4}) \tag{9}$$

where $\omega_p = 2\pi/T_p$ is the wave spectral peak frequency.

The JONSWAP spectrum $S_{JON}(\omega)$, representing a fetch limited developing sea state, can be calculated by

$$S_{JON}(\omega) = (1 - 0.287 \ln(\gamma_p)) S_{PM}(\omega, \omega_p, H_s) \gamma_p^{\exp(-0.5(\frac{\omega-\omega_p}{\sigma_w \omega_p})^2)} \tag{10a}$$

$$\gamma_p = \begin{cases} 5 & \text{for } T_p/\sqrt{H_s} \leq 3.6 \\ \exp(5.75 - 1.15\frac{T_p}{\sqrt{H_s}}) & \text{for } 3.6 < T_p/\sqrt{H_s} < 5 \\ 1 & \text{for } T_p/\sqrt{H_s} \geq 5 \end{cases} \tag{10b}$$

$$\sigma_w = \begin{cases} 0.07 & \text{for } \omega \leq \omega_p \\ 0.09 & \text{for } \omega > \omega_p \end{cases} \tag{10c}$$

where γ_p is the peak enhancement factor calculated based on H_s and T_p, and σ_w is the spectral width parameter.

The double-peaked Torsethaugen spectrum can be calculated based on the simplified form described in Appendix A.2 in DNVGL-RP-C205 (2017). It is the sum of two JONSWAP spectra described in Eq. (10). The simplified formulation of the Torsethaugen spectrum $S_{Tor}(\omega)$ is different for the case of sea states dominated by wind seas versus those dominated by swells. These are distinguished based on the value of the parameter $T_f = 6.6 H_s^{1/3}$:

$$S_{Tor}(\omega) = S_{JON,w}(\omega|H_{s,w}, T_{p,w}, \gamma_{p,w}) + S_{JON,sw}(\omega|H_{s,sw}, T_{p,sw}, \gamma_{p,sw}) \tag{11a}$$

For wind dominated sea ($T_p \leq T_f$):

$$H_{s,w} = r_{pw} H_s \tag{11b}$$

$$T_{p,w} = T_p \tag{11c}$$

$$\gamma_{p,w} = 35[\frac{2\pi}{g} \frac{H_{s,w}}{T_p^2}]^{0.857} \tag{11d}$$

$$H_{s,sw} = \sqrt{1 - r_{pw}^2} H_s \tag{11e}$$

$$T_{p,sw} = T_f + 2.0 \tag{11f}$$

$$\gamma_{p,sw} = 1 \tag{11g}$$

$$r_{pw} = 0.7 + 0.3 \exp(-(2\frac{T_f - T_p}{T_f - 2\sqrt{H_s}})^2) \tag{11h}$$

For swell dominated sea ($T_p > T_f$):

$$H_{s,w} = \sqrt{1 - r_{ps}^2} H_s \tag{11i}$$

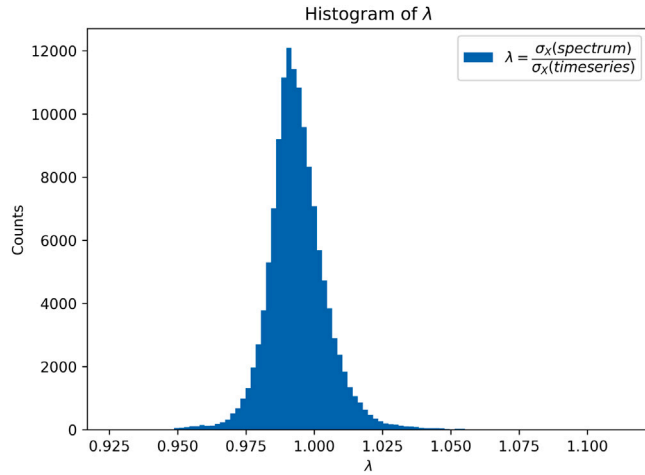$$T_{p,w} = 6.6 H_{s,w}^{1/3} \tag{11j}$$

$$\gamma_{p,w} = 1 \tag{11k}$$

$$H_{s,sw} = r_{ps} H_s \tag{11l}$$

$$T_{p,sw} = T_p \tag{11m}$$

$$\gamma_{p,sw} = 35[\frac{2\pi}{g} \frac{H_s}{T_f^2}]^{0.857}(1 + 6\frac{T_p - T_f}{25 - T_f}) \tag{11n}$$

Table 4
Parameter variation for generating heave response signals.

Parameter	Values	Unit	Number of values
H_s	{1, 4}	m	2
T_p	{5, 6, …, 25}	s	21
β_W	{0, 30, 60, 90}	°	4
Wave spectrum	{PM, JONSWAP, Torsethaugen}	–	3
Seed variation	Random [1, 300]	–	10
SNR	{10, 30, 100}	–	3
Sensor	Described in Table 3	–	9

Fig. 4. Distribution of λ, i.e., the ratio between standard deviations calculated based on the spectrum by Eq. (2a) and the time series by Eq. (1a) without noises.

$$r_{ps} = 0.6 + 0.4 \exp\left(-\left(\frac{T_p - T_f}{0.3(25 - T_f)}\right)^2\right) \tag{11o}$$

where $H_{s,w}$, $T_{p,w}$, and $\gamma_{p,w}$ stand for the associated H_s, T_p, and γ_p of the wind sea component $S_{JON,w}(\omega|H_{s,w}, T_{p,w}, \gamma_{p,w})$, while $H_{s,sw}$, $T_{p,sw}$, $\gamma_{p,sw}$ correspond to the swell component $S_{JON,sw}(\omega|H_{s,sw}, T_{p,sw}, \gamma_{p,sw})$.

A FFT (Cooley and Tukey, 1965) lowpass filter using the Python SciPy package (Virtanen et al., 2020) was applied to filter each signal, by application of many different cutoff frequencies $f_{lp} \in [0.05, 2.0]$ Hz. The optimal cutoff frequency f_{lp}^*, therefore, can be determined by comparing the STD of the filtered signal $\hat{\sigma}_X(f_{lp})$ with the STD of the true response time series σ_X^*. The study tested 25 cutoff frequencies for each signal, i.e., $f_{lp} \in \{0.050, 0.053, 0.056, 0.059, 0.063, 0.067, 0.071, 0.077, 0.083, 0.091, 0.10, 0.111, 0.125, 0.143, 0.167, 0.20, 0.25, 0.30, 0.33, 0.40, 0.50, 0.60, 0.75, 1.0, 1.5, 2.0\}$ Hz.

4. Data exploration

This section aims to identify the most relevant input parameters for the optimal cutoff frequency f_{lp}^* and to propose a way to find f_{lp}^*. Due to the limited number of discretized frequencies and discretized time steps for a given simulation length based on Eq. (8), the generated response time series will not contain exactly the same power as the response power spectrum. Fig. 4 indicates that there may be up to about a ±2.5% error/
uncertainty for the studied 1-h response realizations with a limited number of discrete frequencies and time steps. This approximately corresponds to a SNR of 20. The uncertainty can be reduced by increasing the number of discretized frequencies, reducing the time series sampling interval, and increasing the duration of the realization. The studies did not attempt to reduce this error.

Fig. 5 shows the overall distribution of the optimal cutoff frequency f_{lp}^* together with the 5-, 25-, 50-, 75-, and 95-percentile values. The optimal cutoff frequencies are well concentrated between 0.15 Hz and
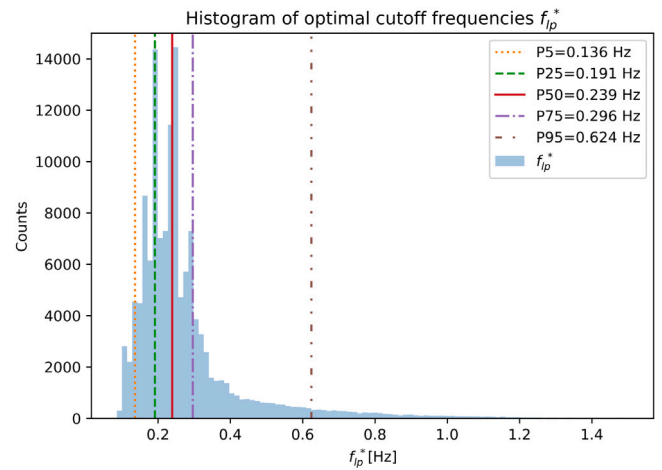
Fig. 5. Histogram of the optimal lowpass filter cutoff frequencies.

0.3 Hz. However, further data exploration has to be performed in order to find any possible relation between f_{lp}^* and the input parameters quantitatively.

Initial data exploration shows that the optimal cutoff frequency f_{lp}^* can be influenced by the characteristic spectral period (e.g., T_p), incoming wave direction β_W, wave spectral shape, the sensor location, and noise level SNR. In addition, the significant influence from seed variation is also observed. The optimal cutoff frequency value from signals with higher SNR (less noise) seems to be more affected by seed variation.

Note that there were very few cases (0.005%) that failed to find an optimal cutoff frequency within the tested range ([0.05, 2.0] Hz), mostly due to the effects from seed variation, and the limitations in accuracy which are associated with numerical calculations based on discrete frequencies and time steps. It only happened for SNR = 100.

Plots show that the function $f_{lp}^*(T_p)$ could be well fitted by a linear function (e.g., $f_{lp}^* = aT_p + b$) or a bi-linear function (e.g., $f_{lp}^* = aT_p + b$ for all $T_p \le T_0$; $f_{lp}^* = cT_p + d$ for all $T_p > T_0$). However, the fitted parameters (e.g., a, b, T_0, etc.) depend on many input parameters, such as β_W, wave spectral shape, sensor location, vessel condition, etc. Therefore, it is difficult to find a clear function for the optimal cutoff frequency directly with respect to the wave and sensor inputs, i.e., $f_{lp}^*(T_p, \beta_W,$ spectral type, sensor, etc.).

4.1. Standard deviation and zero-upcrossing period of filtered signals

Therefore, it is of interest to further investigate details on how the standard deviation (STD) and zero-upcrossing period of the filtered signal ($\hat{\sigma}_X(f_{lp})$ and $\hat{T}_z(f_{lp})$) changes with changing cutoff frequency. For example, Figs. 6 and 7 show that:

1. The optimal cutoff frequency f_{lp}^* always stays at or near the turning point of the $\hat{\sigma}_X$-f_{lp} curve.
2. The optimal cutoff frequency f_{lp}^* is always on the "plateau" of the $\hat{T}_z$-f_{lp} curves, but not necessarily at the turning point.
3. When a larger f_{lp} applies, less noise is filtered out. But $\hat{\sigma}_X(f_{lp})$ increases very slowly with increasing f_{lp} for $f_{lp} > f_{lp}^*$. This means that even though applying larger f_{lp} may lead to biased tuning results, it is still much safer to use a slightly larger f_{lp} than a slightly smaller f_{lp} relative to f_{lp}^*.

The reason for the existence of the "plateau" in the $\hat{T}_z$-f_{lp} curve is the clear distinction between the main frequency regions for the true vessel response versus the signal noise. In addition, the less the noise level is (i.e., larger SNR), the flatter and longer the "plateau" will be.
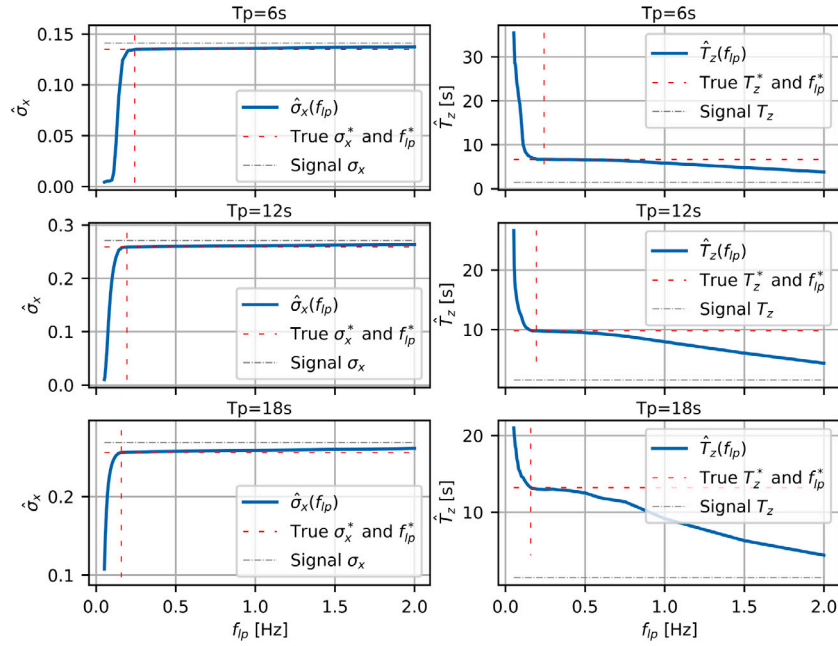
Fig. 6. $\hat{\sigma}_X$-f_{lp} and $\hat{T}_z$-f_{lp} curves for Disp_A sensor, SNR = 10, $\beta_W = 90°$, $T_p = 6$ s, 12 s, and 18 s.
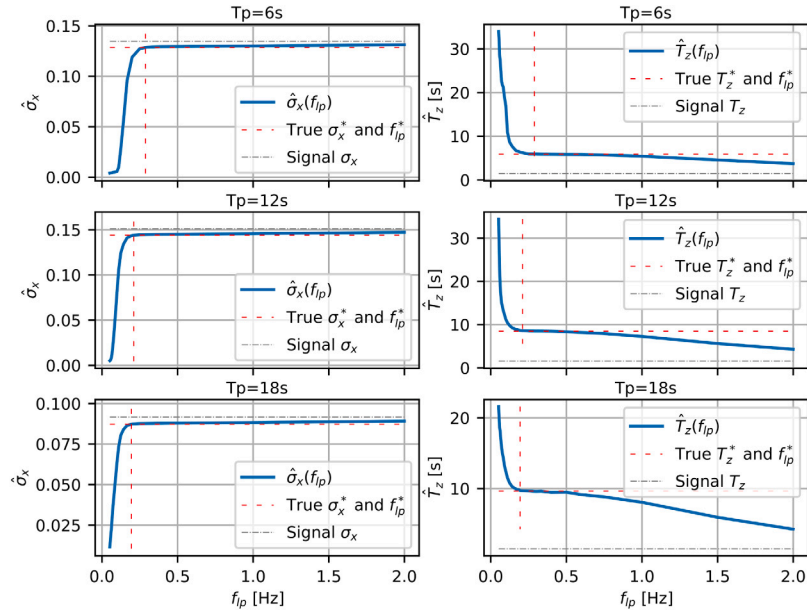

Fig. 7. $\hat{\sigma}_X$-f_{lp} and $\hat{T}_z$-f_{lp} curves for Acc_C sensor, SNR = 10, $\beta_W = 0°$, $T_p = 6$ s, 12 s, and 18 s.

This is because less noise will have less influence on the overall signal zero-upcrossing period.

Therefore, it can be helpful to determine the optimal cutoff frequency based on the characteristics of the $\hat{\sigma}_X$-f_{lp} and $\hat{T}_z$-f_{lp} curves. Two parameters are introduced, representing the absolute values of the normalized slopes of the $\hat{T}_z$ - f_{lp} and $\hat{\sigma}_X$ - f_{lp} curves. The hat operator $\hat{\ }$ means the filtered results.

The efficiency of increasing or reducing the cutoff frequency on the change of the filtered signal energy, is referred to as $\theta(f_{lp})$, defined by

$$\theta\left(f_{lp,i}\right) = \frac{\hat{\sigma}_X\left(f_{lp,i}\right) - \hat{\sigma}_X\left(f_{lp,i-1}\right)}{\hat{\sigma}_X\left(f_{lp,i}\right) \cdot \left(f_{lp,i} - f_{lp,i-1}\right)} \tag{12}$$

where $\hat{\sigma}_X\left(f_{lp,i}\right)$ means the filtered signal STD by application of the cutoff frequency $f_{lp,i}$

The effect of increasing or reducing the cutoff frequency on the change of the zero-upcrossing period of the filtered signal, is referred to as $\lambda\left(f_{lp}\right)$

$$\gamma\left(f_{lp,i}\right) = \frac{\hat{T}_z\left(f_{lp,i-1}\right) - \hat{T}_z\left(f_{lp,i}\right)}{\hat{T}_z\left(f_{lp,i}\right) \cdot \left(f_{lp,i} - f_{lp,i-1}\right)} \tag{13}$$

where $\hat{T}_z\left(f_{lp,i}\right)$ means the zero-upcrossing period of the filtered signal based on the cutoff frequency of $f_{lp,i}$. Please note that γ is positive when the slope of the $\hat{T}_z$-f_{lp} curve is negative. When $\left(f_{lp,i} - f_{lp,i-1}\right) \rightarrow 0$, $\theta\left(f_{lp,i}\right)$ represents the normalized slope of the $\hat{\sigma}_X$-f_{lp} curve at $f_{lp,i}$, while $\gamma\left(f_{lp,i}\right)$ represents the opposite value of the normalized slope of the $\hat{T}_z$-f_{lp} curve at $f_{lp,i}$. The true response STD is in the following defined as σ_X^*.
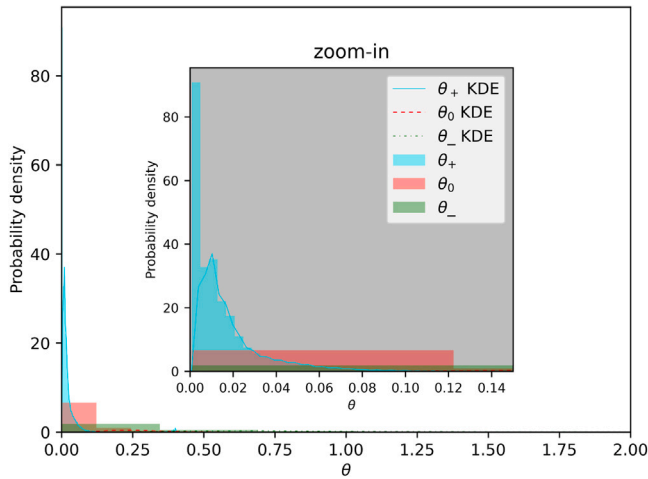
Fig. 8. Normalized histogram of θ_-, θ_0, and θ_+ based on all studied signals. The fitted lines are the estimated Gaussian kernel densities (Waskom et al., 2020) based on the corresponding normalized histograms. KDE: kernel density estimation.

Fig. 9. Normalized histogram of γ_-, γ_0, and γ_+ based on all studied signals. The fitted lines are the estimated Gaussian kernel densities based on the corresponding normalized histograms. KDE: kernel density estimation.

Table 5
Distribution of θ and γ values near the optimal cutoff frequency.

Parameter	P5	P25	P50	P75	P95
f_{lp}^*	0.136	0.191	0.239	0.296	0.624
θ_-	0.0011	0.0258	0.189	0.569	2.263
θ_0	0.001	0.0082	0.0371	0.0989	0.341
θ_+	0.001	0.0033	0.009	0.0181	0.0502
γ_-	−0.111	0.062	0.359	0.961	2.591
γ_0	−0.137	0.000559	0.109	0.285	0.841
γ_+	−0.136	−0.00056	0.053	0.139	0.36

The program tested a limited number of discrete f_{lp} values gradually as described in Section 3.2. Therefore, the optimal frequency is actually found by interpolation between the neighboring frequencies, f_{lp,i^*} and f_{lp,i^*+1}, where $\hat{\sigma}_X\left(f_{lp,i^*}\right) \leq \sigma_X^* \leq \hat{\sigma}_X\left(f_{lp,i^*+1}\right)$ for $f_{lp,i^*} \leq f_{lp}^* \leq f_{lp,i^*+1}$. Due to the mentioned findings of the two curves, the distributions of the θ and γ values around the optimal cutoff frequency f_{lp}^* are of great interest to further investigate, and these are therefore defined as follows:

$$\theta_- = \frac{\hat{\sigma}_X\left(f_{lp,i^*}\right) - \hat{\sigma}_X\left(f_{lp,i^*-1}\right)}{\hat{\sigma}_X\left(f_{lp,i^*}\right) \cdot \left(f_{lp,i^*} - f_{lp,i^*-1}\right)} \tag{14a}$$

$$\theta_0 = \frac{\hat{\sigma}_X\left(f_{lp,i^*+1}\right) - \hat{\sigma}_X\left(f_{lp,i^*}\right)}{\hat{\sigma}_X\left(f_{lp,i^*+1}\right) \cdot \left(f_{lp,i^*+1} - f_{lp,i^*}\right)} \tag{14b}$$

$$\theta_+ = \frac{\hat{\sigma}_X\left(f_{lp,i^*+2}\right) - \hat{\sigma}_X\left(f_{lp,i^*+1}\right)}{\hat{\sigma}_X\left(f_{lp,i^*+2}\right) \cdot \left(f_{lp,i^*+2} - f_{lp,i^*+1}\right)} \tag{14c}$$

$$\gamma_- = \frac{\hat{T}_z\left(f_{lp,i^*-1}\right) - \hat{T}_z\left(f_{lp,i^*}\right)}{\hat{T}_z\left(f_{lp,i^*}\right) \cdot \left(f_{lp,i^*} - f_{lp,i^*-1}\right)} \tag{15a}$$

$$\gamma_0 = \frac{\hat{T}_z\left(f_{lp,i^*}\right) - \hat{T}_z\left(f_{lp,i^*+1}\right)}{\hat{T}_z\left(f_{lp,i^*+1}\right) \cdot \left(f_{lp,i^*+1} - f_{lp,i^*}\right)} \tag{15b}$$

$$\gamma_+ = \frac{\hat{T}_z\left(f_{lp,i^*+1}\right) - \hat{T}_z\left(f_{lp,i^*+2}\right)}{\hat{T}_z\left(f_{lp,i^*+2}\right) \cdot \left(f_{lp,i^*+2} - f_{lp,i^*+1}\right)} \tag{15c}$$

Note that the values of θ and γ can be influenced by the resolution of the tested f_{lp} values. The histograms of the parameters θ_-, θ_0, θ_+, γ_-, γ_0, and γ_+ are shown in Figs. 8 and 9. Because of the large difference between the bin ranges for the parameters (e.g., θ_-, θ_0, and θ_+), the plotted histograms were normalized for the purpose of easier comparison between them. The histogram of each variable considered 100 bins, and the histogram was normalized so that the height (denoted as h) of the histogram plot represents the probability density of the parameter (denoted as v). The bins are evenly distributed, so that $\Delta v = \frac{v_{max} - v_{min}}{100}$. The plotted normalized histogram plots fulfill

$$\sum_{i=1}^{100} h_i \cdot \Delta v = 1.0. \tag{16}$$

It is clear that θ_+ is highly concentrated in a much smaller θ value range, as compared with the distributions of θ_- and θ_0. However, γ_-, γ_0 and γ_+ are all distributed around zero, with γ_+ having the
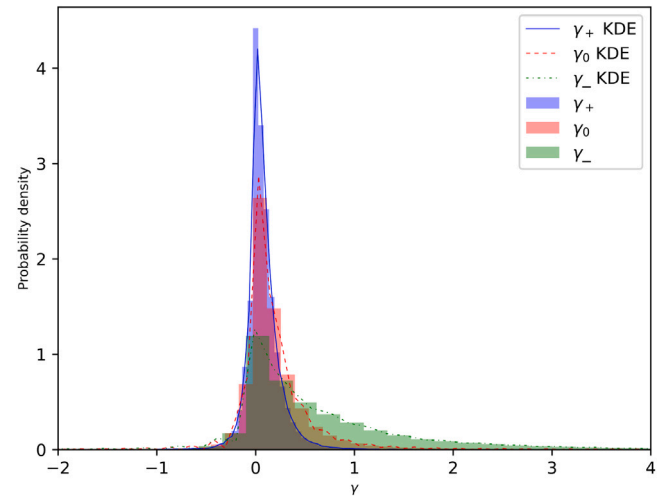
smallest variance. These observations positively support the findings from Figs. 6 and 7. The statistical percentile values of all these 6 parameters are summarized in Table 5.

It is also interesting to find that the uncertainty of $\theta\left(f_{lp}^*\right)$ is highly correlated with the SNR. Larger noise leads to larger variation of $\theta\left(f_{lp}^*\right)$ for different signals (seed variation) from the same response spectrum. However, this does not conflict with the previous findings that higher noise leads to less variation of f_{lp}^* for different signals due to seed variation for the same response spectrum. The distributions of θ_-, θ_0, θ_+ become even more distinguishable for a certain SNR value (e.g., Figs. 10 and 11).

As shown in Table 5 and Fig. 9, the γ values are small and stable near f_{lp}^*, which means that the optimal cutoff is on the "plateau" of the $\hat{T}_z$-f_{lp} curve. As γ_-, γ_0, γ_+ are similarly distributed, the criterion for γ must be relaxed, acting as a supplementary rule for the θ criterion.

4.2. Proposed strategy to find optimal cutoff frequency

Due to the large slope of the $\hat{\sigma}_X$ - f_{lp} curve for $f_{lp} < f_{lp}^*$, it is better to filter slightly less noise than risking to filter out too much energy. Assuming no low-frequency motion, the proposed strategy to find the optimal lowpass filter cutoff frequency f_{lp}^* in order to retain only the signals within the wave frequency region is summarized as follows.

1. Starting from a small cutoff frequency $f_{lp,1}$ of, e.g., 0.02 Hz, filter the noisy signal $x(t)$, and calculate the STD and zero-upcrossing period of the filtered signal, i.e., $\hat{\sigma}_X(f_{lp,1})$ and $\hat{T}_z(f_{lp,1})$.
2. Repeat step 1 by gradually increasing the cutoff frequency $f_{lp,i}, i = 2, 3, \ldots$. Calculate $\hat{\sigma}(f_{lp,i})$, $\hat{T}_z(f_{lp,i})$, $\theta(f_{lp,i})$, and $\gamma(f_{lp,i})$ for $i = 2, 3, \ldots$.
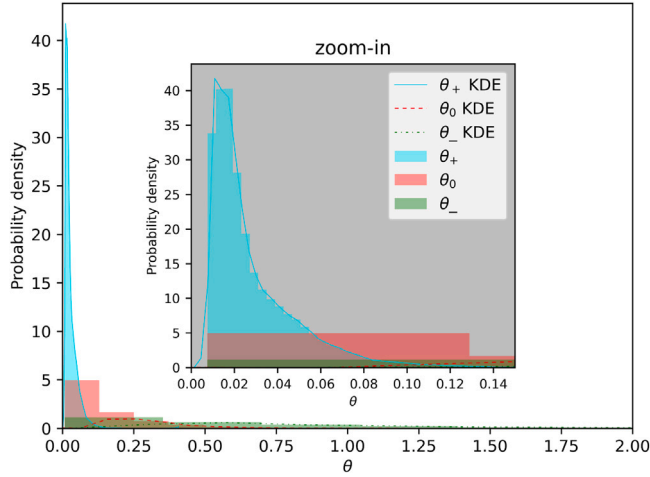
Fig. 10. Normalized histogram of θ_-, θ_0, and θ_+ based on the studied signals for a SNR of 10. The fitted lines are the estimated Gaussian kernel densities based on the corresponding normalized histograms. KDE: kernel density estimation.
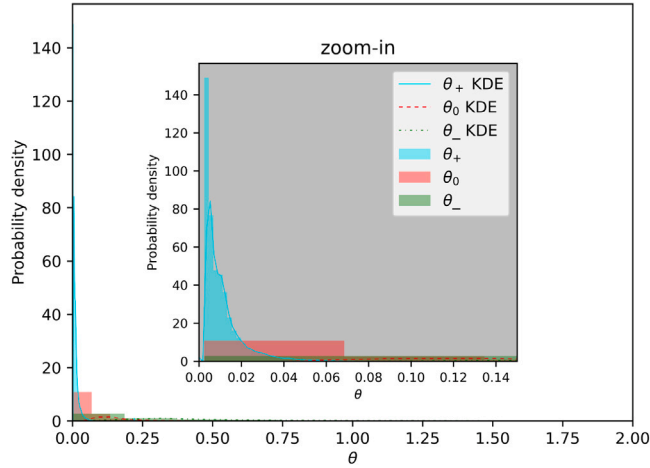

Fig. 11. Normalized histogram of θ_-, θ_0, and θ_+ based on the studied signals for a SNR of 30. The fitted lines are the estimated Gaussian kernel densities based on the corresponding normalized histograms. KDE: kernel density estimation.

3. Then the first cutoff frequency $f_{lp,i*}$ where both the values of $\theta_{f_{lp,i*}}$ and $\gamma_{f_{lp,i*}}$ meet the preset criteria, will be considered as the optimal cutoff frequency, denoted as $\tilde{f}_{lp}^*$.

It is not necessary to explicitly define the "turning" point of the $\hat{\sigma}_X$-f_{lp} curve. When the resolution of the tested f_{lp} is sufficiently fine, θ_0 and θ_+ will be very close, and practically it does not matter which of these values is selected. Based on the statistical distribution of θ and γ summarized in Table 5, the following criteria are considered as the base case.

$$\theta(f_{lp}^*) \leq 0.05 \tag{17a}$$

$$\gamma(f_{lp}^*) \leq 0.9 \tag{17b}$$

The $\theta(f_{lp}^*) \leq 0.05$ was chosen based on statistical information about θ_0 and θ_+ so that θ_+ meets the criterion for 95% of the cases, and more than half of θ_0 meets the criterion. The histograms of θ_-, θ_0, θ_+ indicate that the selected criterion is statistically appropriate.

As the θ and γ criteria are based on statistics of a case study, it cannot guarantee that the present procedure will find the optimal cutoff frequency for all signals. Therefore, one supplementary requirement was introduced to ensure returning an "optimal" cutoff frequency value

for signal filtering, i.e., f_{lp}^* must be within [0.1, 0.9] Hz, i.e.,

$$f_{lp}^* = \begin{cases} 0.1 \text{ Hz}, & \text{if } \tilde{f}_{lp}^* < 0.1 \text{ Hz} \\ 0.9 \text{ Hz}, & \text{if } \tilde{f}_{lp}^* > 0.9 \text{ Hz} \\ \tilde{f}_{lp}^*, & \text{otherwise} \end{cases} \tag{18}$$

where $\tilde{f}_{lp}^*$ means the identified optimal cutoff frequency based on the main proposed strategy with the criteria in Eq. (17). The algorithm are also summarized in pseudo code format.

Algorithm 1: Recursive searching of optimal cutoff frequency.

Initialize: i=0, $\theta = 1.0$, $\gamma = 10.0$;
Input: Predefined f_{lp} values in ascending order and the signal $x(t)$;
while $\theta > 0.05$ *or* $\gamma > 0.9$ **do**
   $i = i + 1$;
   Obtain $\hat{x}(t)$ by filtering $x(t)$ at cutoff frequency of $f_{lp,i}$;
   Calculate $\hat{\sigma}_X(f_{lp,i})$ and $\hat{T}_z(f_{lp,i})$;
   if $i > 1$ **then**
      Calculate $\theta(f_{lp,i})$ by Equation (12) and $\gamma(f_{lp,i})$ by Equation (13);
      $\theta = \theta(f_{lp,i})$;
      $\gamma = \gamma(f_{lp,i})$;
   end
end
$\tilde{f}_{lp}^* = f_{lp,i}$;
if $\tilde{f}_{lp}^* < 0.1 \ Hz$ **then**
   $f_{lp}^* = 0.1 Hz$;
else if $\tilde{f}_{lp}^* > 0.9 \ Hz$ **then**
   $f_{lp}^* = 0.9$ Hz;
else
   $f_{lp}^* = \tilde{f}_{lp}^*$;
end
return f_{lp}^*;

---

5. Test of strategy

5.1. Simulated signals

The proposed strategy was tested for 500 randomly generated vessel motion signals, based on randomly selecting the values of the input parameters summarized in Table 6.

In total, 83 values of $f_{lp} \in [0.06, 5.13]$ Hz were considered for the lowpass filter, as shown in Fig. 12. The resolution was gradually increased with decreasing f_{lp}, especially for $f_{lp} \in [0.1, 0.3]$ Hz.

Different values of θ and γ criteria were also tested, as summarized in Table 7. The parameter κ was defined in order to evaluate the results of the adaptive filtering based on different criteria,

$$\kappa = \frac{\hat{\sigma}_X\left(\tilde{f}_{lp}^*\right)}{\sigma_X^*} \tag{19}$$

where $\hat{\sigma}_X\left(\tilde{f}_{lp}^*\right)$ is the filtered signal STD at the found optimal cutoff frequency $\tilde{f}_{lp}^*$.

Fig. 13 shows the distributions of κ from the 500 test cases (Table 6) for the 4 different sets of criteria (Table 7). Among the results, $\theta = 0.05$ with $\gamma = 0.9$ generally leads to the best filtering results with respect to the response STD, for which the filtered signal STDs are concentrated mostly around the true values. The distribution of κ for Crit2 shows slightly more spreading when using a smaller γ criterion, indicating that γ serves to provide a supplementary criterion for the adaptive filtering process. Results from Crit3 with a much higher θ value are the worst with respect to the filtered signal STD. The distribution is dramatically skewed to the left, indicating that many signals were over-filtered. This is due to a too "relaxed" θ criterion. Crit4 is most strict,

Table 6
Applied parameters related to the strategy test for the adaptive lowpass filter.

Parameter	Values	Unit
H_s	Uniformly distributed in [1.0, 4.0]	m
T_p	Uniformly distributed in [5.0, 22.0]	s
β_W	Randomly selected among 13 discrete directions within [0,180]	°
Seed	Uniformly distributed in [1, 300]	–
Duration	3600	s
SNR[a]	Randomly selected among 15 discrete values within $[int(5 \times 1.2^i), i \in [0, 15]]$	–
Vessel condition	Randomly selected among 10 vessel conditions within the RAO database	–
Sensor	Randomly selected among the 9 sensors described in Table 3	–

[a]The discrete SNR values are determined with approximately 20% difference between neighboring values, for SNR∈ [5, 64].
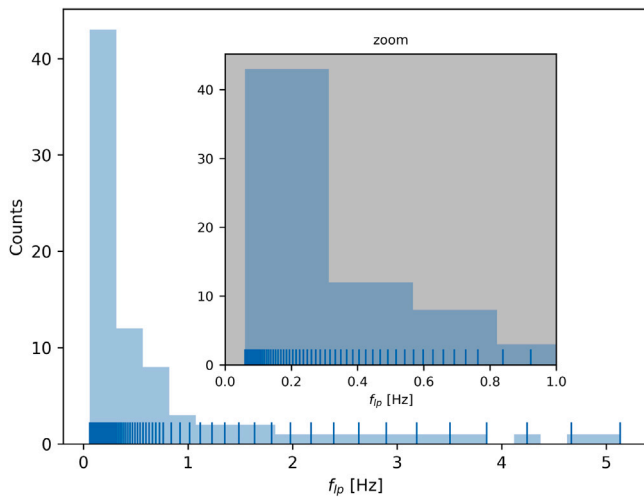
Fig. 12. Histogram of tested f_{lp} values. The blue sticks along the f_{lp} axis represent the data points.

Table 7
Tested θ and γ criteria.

| Case ID	θ	γ
Crit1	0.05	0.9
Crit2	0.05	0.36
Crit3	0.3	0.9
Crit4	0.02	0.2

which, however, did not lead to better filtering results than the base case (Crit1). It can be seen in Fig. 13 that there is a notable skewing to the right, indicating that the signals may be under-filtered.

5.2. On-site MRU measurements

It is interesting to test the proposed strategy by application of on-site measurements. However, it is impossible to know the vessel's true on-site response due to the inevitable measurement uncertainties (Hubbard, 2014). Therefore, it was only possible to test whether or not the $\hat{\sigma}_X$ - f_{lp} and $\hat{T}_z$ - f_{lp} curves show similar characteristics as described in Section 4.1, and to discuss the limitations. It is worth mentioning that the vessel motion signals obtained from MRU are already filtered through, e.g., application of an extended Kalman filter, to avoid drift.

5.2.1. Gunnerus seakeeping and DP tests

The MRU measurements of the NTNU research vessel Gunnerus during seakeeping and DP tests in 2013 (Steen et al., 2016) were
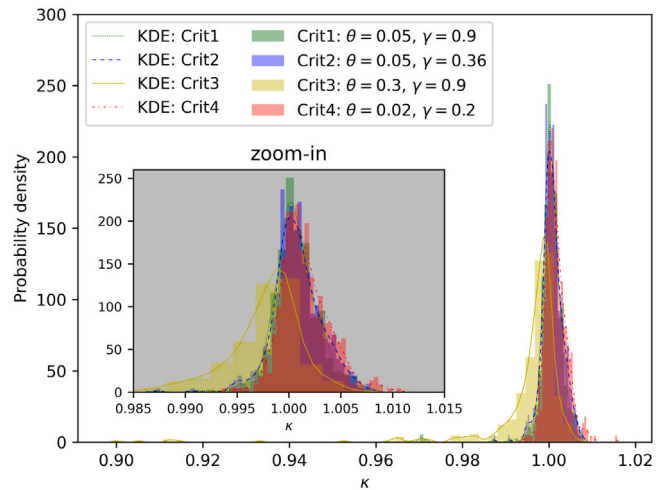
Fig. 13. Normalized histograms of κ values for the strategy test with different criteria. The fitted lines are the estimated Gaussian kernel densities based on the corresponding normalized histograms (Waskom et al., 2020).
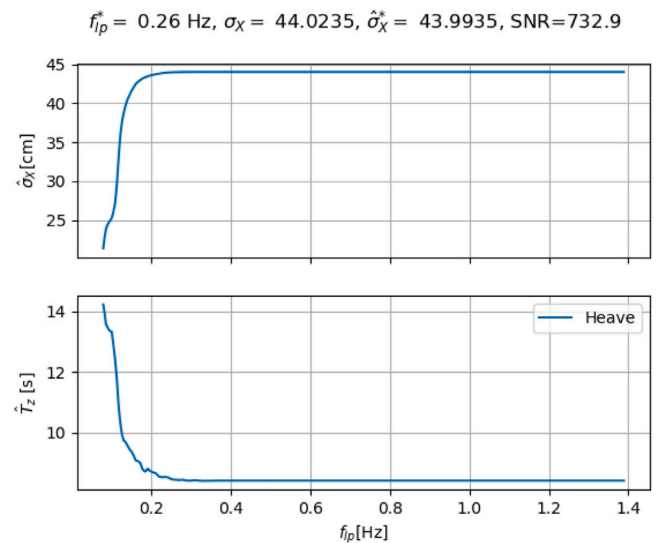
Fig. 14. $\hat{\sigma}_X$ - f_{lp} and $\hat{T}_z$ - f_{lp} curves of heave motion for CaseA1.

considered. Two test cases were reported, one 2-hour DP test (CaseA1) under a sea state with 2 significant peak periods (8.5 s and 13.3 s), and one half-hour seakeeping test (CaseA2) with 10.4kn speed under a swell-dominated sea state.

The quickly reduced slopes of the $\hat{\sigma}_X$-f_{lp} curves were observed for both cases for all MRU measurements with respect to heave, pitch, and roll, e.g., Fig. 14. Because the received MRU signals were already filtered, the noise level was low, as expected. In addition, Gunnerus is a research vessel with a relatively small dimension (about 30 m long), and accordingly its resonance response periods are relatively small. Therefore, the $\hat{T}_z$-f_{lp} curves, as expected, becomes very flat when the cutoff frequency is sufficiently large.

It is interesting to observe the reduced slopes for the $\hat{\sigma}_X$-f_{lp} and $\hat{T}_z$-f_{lp} curves within the wave frequency region for heave and pitch measurements (e.g., Fig. 15). This is because CaseA2 was a swell-dominated sea condition (T_p = 13.5 s) with a small wind sea. The vessel was mostly excited within a relatively low frequency region, while the vessel response resonance was in a relatively high frequency region due to Gunnerus' small dimensions. Therefore, there was a clear gap with respect to the frequencies of the excited vessel motion by the swell and the wind sea.
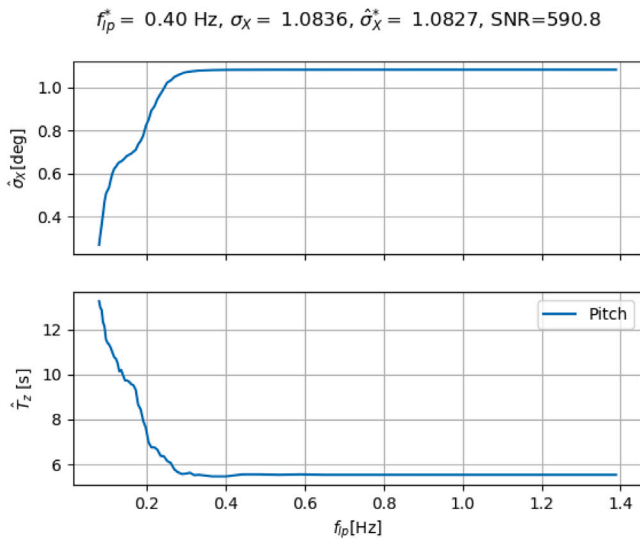
$$f_{lp}^* = 0.40 \text{ Hz}, \sigma_X = 1.0836, \hat{\sigma}_X^* = 1.0827, \text{SNR}=590.8$$

Fig. 15. $\hat{\sigma}_X$ - f_{lp} and $\hat{T}_z$ - f_{lp} curves of pitch motion for CaseA2.

$$f_{lp}^* = 0.19 \text{ Hz}, \sigma_X = 0.3595, \hat{\sigma}_X^* = 0.3592, \text{SNR}=673.1$$

Fig. 16. $\hat{\sigma}_X$ - f_{lp} and $\hat{T}_z$ - f_{lp} curves of pitch motion for CaseB1.

$$f_{lp}^* = 0.15 \text{ Hz}, \sigma_X = 0.7104, \hat{\sigma}_X^* = 0.7096, \text{SNR}=447.8$$
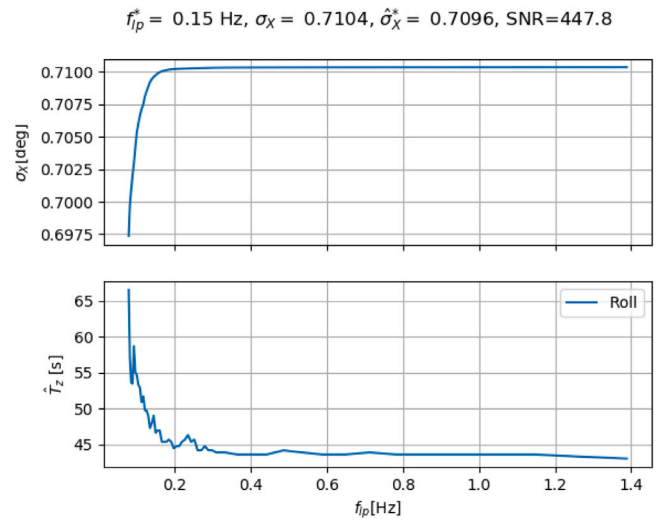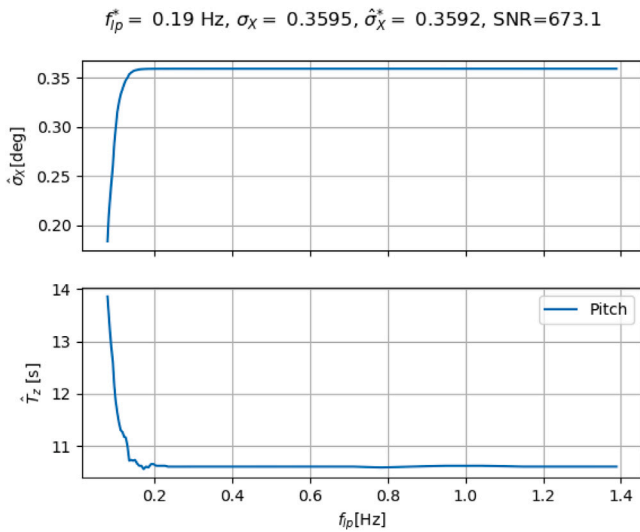
Fig. 17. $\hat{\sigma}_X$ - f_{lp} and $\hat{T}_z$ - f_{lp} curves of roll motion for CaseB1.
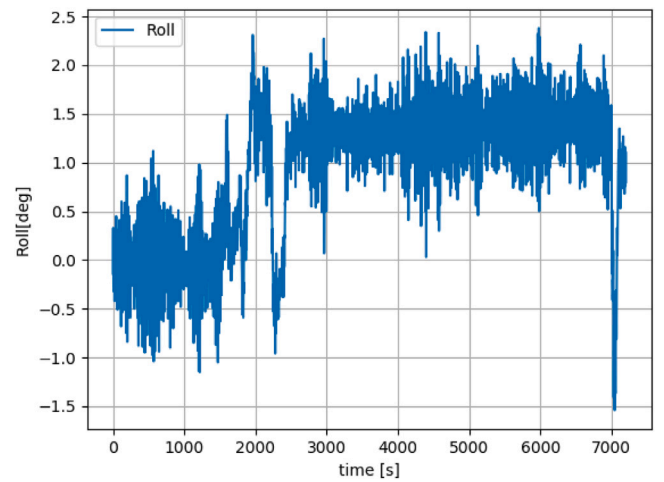
Fig. 18. Time series of roll motion for CaseB1.

5.2.2. Normand vision

The MRU measurements (CaseB1) from Normand Vision during a lifting operation in 2017 were also tested. The operation lasted for a total of 2 hours. The $\hat{\sigma}_X$ - f_{lp} and $\hat{T}_z$ - f_{lp} curves for the 2-hour pitch and roll responses are shown in Figs. 16 and 17. The $\hat{T}_z$ - f_{lp} curve for pitch is not smooth near the turning point. For roll motion, the $\hat{T}_z$ - f_{lp} curve shows an oscillatory behavior, with the $\hat{T}_z$ value converging around 44 s which is larger than the wave periods.

A closer look at the time series of pitch and roll motions indicates that the unstable behavior of the $\hat{T}_z$ - f_{lp} curves were due to the additional low-frequency motion caused by the lift-off and landing operations, see Fig. 18. Consequently as shown in Fig. 19, the vessel trim was also changed due to the change of vessel CoG during the operation.

Then a highpass filter with cutoff frequency of 0.04 Hz was applied to filter out the low-frequency motions before applying the adaptive lowpass filter. The updated $\hat{\sigma}_X$ - f_{lp} and $\hat{T}_z$ - f_{lp} curves of roll motion are shown in Fig. 20. Compared with Fig. 17, the $\hat{T}_z$ - f_{lp} curve in Fig. 20 becomes smoother and converges to a reasonable value.
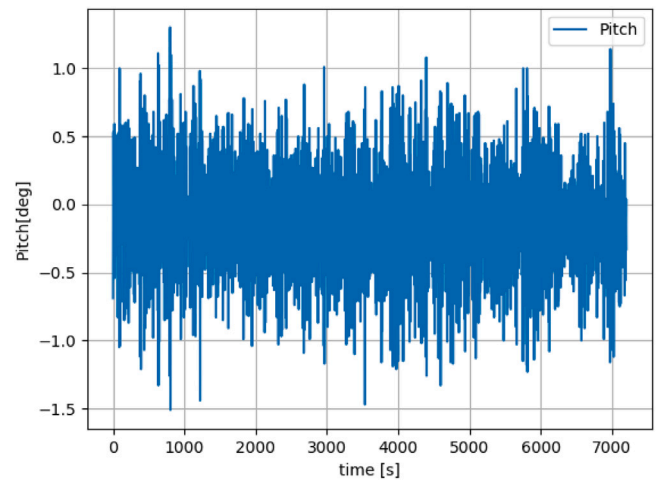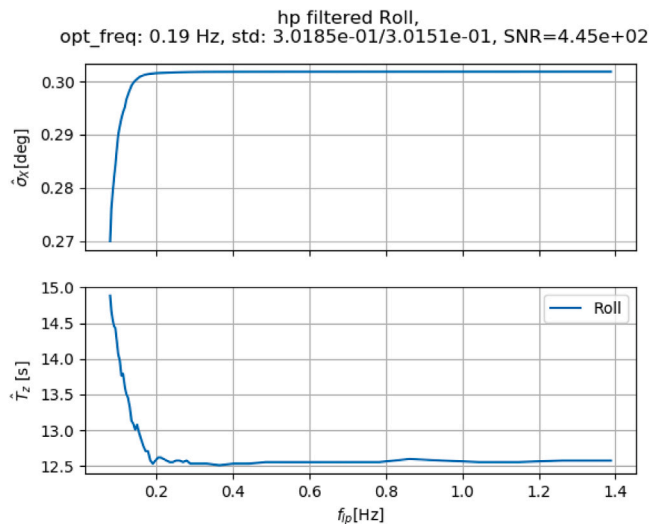

Fig. 19. Time series of pitch motion for CaseB1.

Fig. 20. $\hat{\sigma}_X$ - f_{lp} and $\hat{T}_z$ - f_{lp} curves of the highpass filtered roll motion for CaseB1.

Table 8
Applied parameters related to the model tuning process for method validation.

Parameter	Value	Unit
H_s	Uniformly distributed in [1.0, 4.0]	m
T_p	Uniformly distributed in [5.0, 20.0]	s
β_W	Randomly selected among 13 discrete directions within [0,180]	°
Seeds	Randomly generated within [1,300][a]	-
Duration	3600	s
SNR	Randomly selected among [5, 10, 20, 40, 80]	–
α	0.05	–
p	0.4	–

[a]Two seeds were generated for each sea state. One was applied for the generation of true response time series, the other was applied in order to add noise to the signal.

5.3. Influence on the model tuning results

So far, the proposed adaptive lowpass filter has been shown to be stable with respect to variation of sea states, vessel conditions and noise levels. This section focuses on investigating how much benefit the model tuning can get from the adaptive lowpass filter with the proposed procedure of finding the optimal cutoff frequency. In total, 200 model tuning cases were run with both the adaptive lowpass filter and a lowpass filter with a fixed cutoff frequency of 1.0 Hz. Each model tuning case used vessel response measurements and wave information from 6 randomly generated sea states. The main wave information, the parameters applied to generating measurements, and the parameters used for model tuning are summarized in Table 8. The true vessel condition and the initial probability distributions of the considered vessel model parameters are summarized in Table 9, which is different from the considered vessel condition for algorithm development described in Section 3.2 and Section 4. It is worth mentioning that the important uncertain vessel parameter β_{44}, representing the ratio between the additional (mainly caused by viscous effect) and critical roll damping, actually varies with sea states (Han et al., 2021b). However, a constant true value of β_{44} was considered for simplicity. The considered vessel parameters were tuned simultaneously.

Compared with the model tuning results with a fixed cutoff frequency of 1.0 Hz, the results show that the adaptive filter approach statistically improved the accuracy with respect to the expected values (see Fig. 21) and reduced the variance of the considered parameters

Table 9
Prior information and true values of the considered vessel parameters.

Parameter	Mean	σ^2	$\pm 3\sigma$	True value	Ik[a]	Im[b]
GMT [m]	0.5	0.015	[0.13, 0.87]	0.4	40	6
β_{44}	0.07	4.0E−04	[1%, 13%]	0.04	50	7
r_{55} [m]	32.5	1.0	[29.5, 35.5]	30.55	30	7
XCG [m]	59.4	1.21	[56.1, 62.7]	61.4	30	5

[a]Number of discrete variable values for the joint probability model.
[b]Number of discrete parameter values used in the RAO database.

(see Fig. 22). However, the improvements of the less sensitive parameters (GMT and r_{55}) were not very significant, particularly in terms of the tuned expected values.

6. Conclusions and future work

An algorithm to find the sea state and vessel dependent optimal cutoff frequency for a lowpass filter has been proposed, to improve extracting vessel motions in the wave frequency region from the noisy vessel motion measurement signals. It is difficult to find and express the explicit relation between the optimal cutoff frequency and the characteristics of the sea state, vessel dimensions, and vessel condition. In addition, the environmental uncertainties are difficult to measure, quantify, and control. The proposed algorithm significantly eases these challenges by introducing two parameters θ and γ, based on the statistical characteristics of the $\hat{\sigma}_X$ - f_{lp} and $\hat{T}_z$ - f_{lp} curves around the optimal cutoff frequencies, and these characteristics are not explicitly linked to any sea state or vessel property.

Applying the algorithm to the vessel model tuning process, statistically improves the tuning results, however, to a limited degree for some parameters due to (1) the numerical errors from STD calculations of vessel motions based on discrete time series and spectral densities; and (2) the fact that the considered parameters (e.g., GMT and r_{55}) may not be very sensitive to the involved sea states. The improvements in relation to tuning of β_{44} and XCG are rather significant because they are more sensitive to the considered vessel motions at the involved sea states.

It has been found important to choose a reasonable set of criteria for θ and γ. A relaxed θ criterion can lead to significant signal over-filtering, while too strict criteria may cause the signal under-filtered. Too strict criteria may also make the algorithm fail to find the optimal cutoff frequency based on the proposed normal procedure. Even though the capability of extending the algorithm and the preset θ and γ criteria for other vessel conditions and dimensions has not been fully demonstrated, all the validation tests described in Section 5 used either different vessel conditions (i.e., Sections 5.1 and 5.3) or different vessels (i.e., Section 5.2), rather than the one used for deriving the algorithm (Section 4). This tends to support the hypothesis that the proposed adaptive lowpass filter would work for different vessels and vessel conditions. Section 5 showed that the algorithm is stable and the on-site full-scale measurements also fulfill the characteristics of the $\hat{\sigma}_X$ - f_{lp} and $\hat{T}_z$ - f_{lp} curves as described in Section 4.1. The algorithm works because:

1. The vessel itself is by nature a lowpass filter of the wave energy. Therefore, the high-frequency response normally has much less energy.
2. The noise mainly carries energy in the high-frequency domain distinguishably outside of the frequency region for the main vessel response. Sensor misalignment and bias are slowly varying, i.e., with low frequencies.
3. Signal noise has considerably less energy compared with the true vessel response energy. The SNR values applied for all presented case studies were higher than 5.
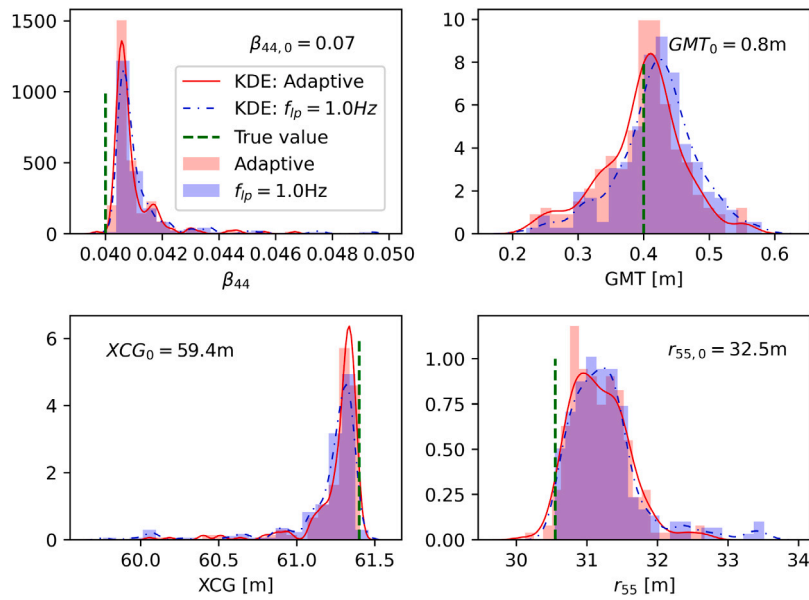
Fig. 21. Normalized histograms (vertical axes) of the expected values for the tuned vessel parameters, comparing the adaptive filter approach with use of a fixed cutoff frequency $f_{lp} = 1.0$ Hz. The red and blue lines are the corresponding estimated Gaussian kernel densities. KDE: kernel density estimation. The parameters with subscript of 0 in the legends refer to the initial values.
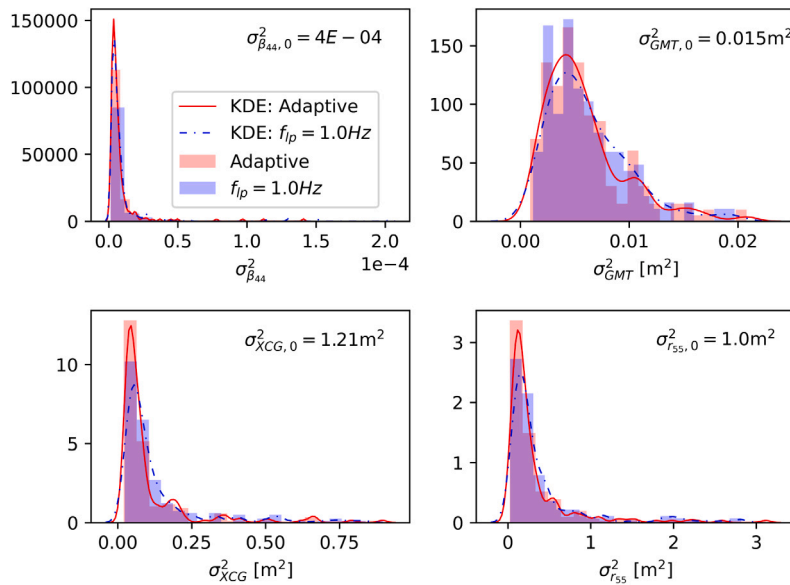

Fig. 22. Normalized histograms (vertical axes) of the variances for the tuned vessel parameters, comparing the adaptive filter approach with use of a fixed cutoff frequency $f_{lp} = 1.0$ Hz. The red and blue lines are the corresponding estimated Gaussian kernel densities. KDE: kernel density estimation. The parameters with subscript of 0 in the legends refer to the initial values.

The proposed adaptive filter algorithm is believed to be a flexible solution, because:

1. It does not require to know the weather or vessel conditions.
2. It is not directly linked to any specific filter. The algorithm uses properties of the standard deviation and zero-upcrossing period of the filtered signal which are available for most signal filters. Even though the present study made use of the FFT filter, the method can be applied based on any other normal filters of any order, as long as the cutoff frequency of that filter model can be explicitly expressed.
3. It does not strictly require a stationary condition. It has been demonstrated in Section 5.2.2 that the $\hat{\sigma}$-f_{lp} and $\hat{T}_z$-f_{lp} curves for the non-stationary signals are similar to the curves for stationary signals (e.g., as illustrated in Figs. 6 and 7) as discussed in

Section 4.1. However, special attention should be paid to those non-stationary conditions which may introduce low-frequency components with high energy.
4. It is expected to be stable at least for vessels with similar dimensions and displacement.

More comprehensive analyses should be performed to verify that the proposed adaptive lowpass filter and its preset θ and γ criteria work for other and significantly different vessels and vessel conditions. The proposed adaptive lowpass filter requires that the power of the response spectrum should be sufficient in magnitude for frequencies less than the optimal cutoff frequency. For a sea state consisting of one wind sea component with a small $T_{p,w}$ and one swell component with a large $T_{p,sw}$ and with two different directions, there might be no wave energy in some periods between $T_{p,w}$ and $T_{p,sw}$. The proposed

method might fail if the search for f_{lp}^* stops immediately after fulfilling the criteria with respect to θ and λ. However, this could be solved by continuously checking the θ and γ values with increasing f_{lp}, ensuring all the considered f_{lp} values larger than f_{lp}^* meet the preset θ and γ criteria as well. Alternatively, the algorithm can be modified so that searching f_{lp}^* starts from the smaller wave spectral peak period (e.g., corresponding to f_{lp} of $1/T_{p,w}$ Hz).

The cases of model tuning considered four uncertain vessel parameters. The interpolation and multiplication operators within the 4-dimensional space requires a significant amount of computer memory. In reality, additional uncertain parameters should be included in the algorithm of model tuning, e.g., vessel heading, vessel speed and wave spectrum related parameters such as H_s, T_p, β_W, directional spreading, etc. As a consequence, the methodology could face the common challenge referred to as the curse of dimensionality in connection with discrete Bayesian inference (Gelman et al., 2013). Modification of the model tuning algorithm should be considered in the future in order to improve the computational efficiency, e.g., by only taking into account the mean vector and covariance matrix of the uncertain vessel parameters (Han et al., 2021c).

CRediT authorship contribution statement

Xu Han: Conceptualization, Methodology, Software, Formal analysis, Data curation, Writing - original draft & editing. **Zhengru Ren:** Writing - review & editing. **Bernt Johan Leira:** Writing - review & editing, Supervision, Project administration, Funding acquisition. **Svein Sævik:** Writing - review & editing, Supervision, Project administration.

Declaration of competing interest

The authors declare that they have no known competing financial interests or personal relationships that could have appeared to influence the work reported in this paper.

Acknowledgments

References

Butterworth, S., 1930. Experimental wireless and the wireless engineer. Wireless Eng. 7, 536.

Challa, S., Bar-Shalom, Y., 2000. Nonlinear filter design using fokker-Planck-Kolmogorov probability density evolutions. IEEE Trans. Aerosp. Electron. Syst. 36 (1), 309–315.

Cooley, J.W., Tukey, J.W., 1965. An algorithm for the machine calculation of complex fourier series. Math. Comp. 19 (90), 297–301.

DNV, 2018. Wasim User Manual. Technical Report, DNV.

DNVGL-RP-C205, 2017. Environmental conditions and environmental loads. Technical Report, DNV.

DNVGL-ST-N001, 2016. Marine operations and marine warranty. Technical Report, DNV.

Fossen, T.I., 2011. Handbook of Marine Craft Hydrodynamics and Motion Control. John Wiley & Sons.

Fossen, T.I., Strand, J.P., 1999. Passive nonlinear observer design for ships using Lyapunov methods: full-scale experiments with a supply vessel. Automatica 35 (1), 3–16.

Gelman, A., Carlin, J., Stern, H., Dunson, D., Vehtari, A., Rubin, D., 2013. Bayesian Data Analysis. CRC press.

Godhaven, J.-M., 1998. Adaptive tuning of heave filter in motion sensor. In: IEEE Oceanic Engineering Society. OCEANS'98. Conference Proceedings (Cat. No.98CH36259), Vol. 1. pp. 174–178.

Grewal, M.S., Henderson, V.D., Miyasako, R.S., 1991. Application of Kalman filtering to the calibration and alignment of inertial navigation systems. IEEE Trans. Automat. Control 36 (1), 3–13. http://dx.doi.org/10.1109/9.62283.

Grip, H.F., Fossen, T.I., Johansen, T.A., Saberi, A., 2015. Globally exponentially stable attitude and gyro bias estimation with application to GNSS/INS integration. Automatica 51, 158–166.

Han, X., Leira, B.J., Sævik, S., 2021a. Vessel hydrodynamic model tuning by discrete Bayesian updating using simulated onboard sensor data. Ocean Eng. 220, http://dx.doi.org/10.1016/j.oceaneng.2020.108407.

Han, X., Leira, B.J., Sævik, S., Ren, Z., 2021c. Onboard tuning of vessel seakeeping model parameters and sea state characteristics. Mar. Struct. 78, http://dx.doi.org/10.1016/j.marstruc.2021.102998.

Han, X., Sævik, S., Leira, B.J., 2020. A sensitivity study of vessel hydrodynamic model parameters. In: Proceedings of the ASME 2020 39th International Conference on Ocean, Offshore and Arctic Engineering, Vol. 1. Virtual, Online.

Han, X., Sævik, S., Leira, B.J., 2021b. Tuning of vessel parameters including sea state dependent roll damping. Ocean Eng. 233, http://dx.doi.org/10.1016/j.oceaneng.2021.109084.

Hubbard, D.W., 2014. How to Measure Anything. John Wiley & Sons, Ltd.

Kring, D.C., 1994. Time Domain Ship Motions by a Three-Dimensional Rankine Panel Method (Ph.D. thesis). Massachusetts Institute of Technology, Doctor of Philosophy in Hydrodynamics, May 1994, Department of Ocean Engineering.

Lewandowski, E.M., 2004. The Dynamics of Marine Craft: Maneuvering and Seakeeping, Vol. 22. World scientific.

Li, W., Wang, J., 2013. Effective adaptive Kalman filter for MEMS-IMU/magnetometers integrated attitude and heading reference systems. J. Navig. 66 (1), 99–113.

Ren, Z., Skjetne, R., Jiang, Z., Gao, Z., Verma, A.S., 2019. Integrated GNSS/IMU hub motion estimator for offshore wind turbine blade installation. Mech. Syst. Signal Process. 123, 222–243.

Scheick, J.T., 1997. Linear Algebra with Applications, Vol. 81. McGraw-Hill New York.

Simon, D., 2006. Optimal State Estimation. John Wiley & Sons, Ltd.

Steen, S., Selvik, Ø., Hassani, V., 2016. Experience with rim-driven azimuthing thrusters on the research ship Gunnerus, In: Proc. of High-Performance Marine Vessels.

Stovner, B.N., Johansen, T.A., Fossen, T.I., Schjølberg, I., 2018. Attitude estimation by multiplicative exogenous Kalman filter. Automatica 95, 347–355.

Virtanen, P., Gommers, R., Oliphant, T.E., Haberland, M., Reddy, T., Cournapeau, D., Burovski, E., Peterson, P., Weckesser, W., Bright, J., van der Walt, S.J., Brett, M., Wilson, J., Jarrod Millman, K., Mayorov, N., Nelson, A.R.J., Jones, E., Kern, R., Larson, E., Carey, C., Polat, İ., Feng, Y., Moore, E.W., Vand erPlas, J., Laxalde, D., Perktold, J., Cimrman, R., Henriksen, I., Quintero, E.A., Harris, C.R., Archibald, A.M., Ribeiro, A.H., Pedregosa, F., van Mulbregt, P., Contributors, S..., 2020. Scipy 1.0: Fundamental algorithms for scientific computing in python. Nature Methods 17, 261–272.

Waskom, M., Botvinnik, O., Ostblom, J., Gelbart, M., Lukauskas, S., Hobson, P., Gemperline, D.C., Augspurger, T., Halchenko, Y., Cole, J.B., Warmenhoven, J., de Ruiter, J., Pye, C., Hoyer, S., Vanderplas, J., Villalba, S., Kunter, G., Quintero, E., Bachant, P., Martin, M., Meyer, K., Swain, C., Miles, A., Brunner, T., O'Kane, D., Yarkoni, T., Williams, M.L., Evans, C., Fitzgerald, C., Brian, 2020. Mwaskom/seaborn: v0.10.1 (april 2020). http://dx.doi.org/10.5281/zenodo.3767070.

Wiener, N., 1964. Extrapolation, Interpolation, and Smoothing of Stationary Time Series. The MIT Press.

Zhang, P., Gu, J., Milios, E.E., Huynh, P., 2005. Navigation with IMU/GPS/digital compass with unscented Kalman filter. In: IEEE International Conference Mechatronics and Automation, 2005, Vol. 3. IEEE, pp. 1497–1502.